Research Square

Preprints are preliminary reports that have not undergone peer review.
They should not be considered conclusive, used to inform clinical practice,
or referenced by the media as validated information.

Flow Excursion and Mixing in the Kneading Block Section of Hot- Melt Extrusion Induced by Carrier Density Variation

Qi Shen
Wenzhou University
Wutong Wu
Zhejiang Canaan Technology Co., Ltd
Huagui Li
Zhejiang Petrochemical Valves Co., Ltd.
Yibiao Chen
chenyibiao212@163.com
Wenzhou University
Hongming Zhou
Wenzhou Polytechnic College

Research Article

Keywords: Hot melt extrusion, Kneading block, Carrier density, Fluid excursion, Mixing

Posted Date: August 21st, 2026

DOI: https://doi.org/10.21203/rs.3.rs-10488753/v1

License: This work is licensed under a Creative Commons Attribution 4.0 International License.
Read Full License

Additional Declarations: No competing interests reported.

Qi Shen，Wutong Wu，Huagui Li，Yibiao Chen*，Hongming Zhou

Flow Excursion and Mixing in the Kneading Block Section of Hot-Melt Extrusion Induced by Carrier Density Variation

Qi Shen:
Wenzhou University, Wenzhou, China, School of Mechanical and Electrical Engineering
e-mail：13675730473@163.com

Wutong Wu:
Zhejiang Canaan Technology Co., Ltd, Whenzhou, China
e-mail：tomwu@china-jianan.com

Huagui Li:
Zhejiang Petrochemical Valves Co., Ltd., Whenzhou, China
e-mail：15868760688@163.com

Yibiao Chen(Corresponding authors):
Wenzhou University, Wenzhou, China, School of Mechanical and Electrical Engineering
e-mail：chenyibiao212@163.com

Hongming Zhou:
Wenzhou Polytechnic College, Whenzhou, China
e-mail：zhm69314@163.com

Flow Excursion and Mixing in the Kneading Block Section of Hot-Melt Extrusion Induced by Carrier Density Variation

abstract

With the increasingly widespread use of poorly soluble active pharmaceutical ingredients (API), hot melt extrusion (HME) technology develop rapidly in the pharmaceutical industry as a highly efficient method for preparing solid dispersions of insoluble drugs. Currently, the selection of carrier materials in pharmaceutical production largely relies on experimental trial-and-error, and the influence of specific material parameters—such as carrier density—on the mixing process remains unclear. By employing Computational Fluid Dynamics (CFD) simulations of fluid flow under simplified ideal conditions, this study analyzes the effects of variations in carrier materials on the flow and mixing processes within the kneading block zone of a hot-melt extruder. When the API and carrier fluids are subjected to compression, relative movement occurs between them, resulting in flow excursion. The disparity in carrier density and the shear force variation across the kneading block zone amplifies this excursion, thereby influencing mixing efficiency.

Keywords: Hot melt extrusion, Kneading block, Carrier density, Fluid excursion, Mixing.

1 Introduction

With the growing demand for pharmaceuticals, enhancing production efficiency while ensuring quality has become a central objective in the pharmaceutical industry.

Compared with sectors such as food and industrial materials, pharmaceutical processes and manufacturing require more stringent monitoring and control. Efficient and precise continuous manufacturing represents a critical pathway for the advancement of pharmaceutical technology[1]. Currently, more than 50% of the API used in the drug market belong to Biopharmaceutics Classification System Class II, characterized by poor aqueous solubility, which consequently leads to low bioavailability in formulations[2,3]. Therefore, developing processes and formulations capable of enhancing the solubility and bioavailability of these compounds is crucial. As an efficient, continuous, and solvent-free processing method, HME technology has been widely applied in fields such as polymer material modification, pharmaceutical solid dispersion preparation, food processing, and advanced composite material synthesis [4,5]. Its core advantages lie in its powerful mixing capability, precise process control (temperature, shear, residence time), and suitability for heat-sensitive materials [6–9]. Achieving an ideal mixing state is essential for the successful application of twin-screw extrusion. This process relies on the intensive dispersive and distributive mixing action exerted by the complex flow fields (including shear and extensional flows) within the extruder on the material.

Therefore, numerous researchers have investigated the fluid flow and mixing behavior during HME to examine the influence of process parameters on mixing performance within the extruder. In experimental studies, Monschke et al. [10] and Ren et al. [11] investigated the influence of process parameters such as torque, kneading element angle, screw speed, and feed rate on mixing outcomes. Hanada et al. [12] demonstrated that increasing the specific mechanical energy, calculated from torque, feed rate, and screw speed, enhances the miscibility between the polymer and the API. Dhenge et al. [13], Srinivasan et al. [14] and Radhan et al. [15] employed methods such

as tracer experiments, differential scanning calorimetry (DSC), Fourier-transform infrared spectroscopy (FTIR), scanning electron microscopy (SEM), in vitro release testing, drug content analysis, and stability studies to investigate the effects of process parameters like fluid motion and overflight clearance during mixing.

With the advancement of computational numerical simulation software, many researchers have begun utilizing CFD to model the dynamics within twin-screw extrusion processes. Eitzlmayr et al. [4] and Ufodike et al. [16] utilized CFD, integrating experimental and numerical calculations, to propose flow dynamics models applicable to different conditions. Song et al. [17] and Qin et al. [18] conducted multi-physics simulations to analyze the influence mechanisms of viscosity characteristics and structural parameters on transient flow field characteristics and mixing performance during extrusion. Suwardie et al. [19] employed oscillatory and capillary rheometers to determine the dynamic and steady-state viscosity of APAP/PEO mixtures. The results proved that at high shear rates, the mixture exhibits shear-thinning behavior, with reduced sensitivity of viscosity to drug loading. And thus the viscosity data under high shear rates better represent the material's rheological behavior during extrusion. Tianwen Dong et al. [20] simulated the flow and mixing behavior of high-viscosity fluids in conveying elements of twin-screw extruders using a parallelized smoothed particle hydrodynamics (SPH) method.

In the design of extrusion processes and the selection of materials [21], the influence of density differences on the mixing process in TSE has not yet been systematically and thoroughly investigated. In practical formulations, a single API can be formulated with a variety of different carrier materials. Beyond differences in physical properties like viscosity and permeability, and chemical properties such as melting point, distinct polymeric carriers suitable for the same API also frequently

exhibit significant density variations. For example, during the production of an indomethacin dispersion, the density of the molten API is 1.32 g/cm³, a range of carrier materials with densities ranging from approximately 1 g/cm³ to 1.3 g/cm³ are available for selection. In pharmaceutical HME, the rheological behavior of the API and carrier fluid can be described by the Bird-Carreau model [22]. In Carreau non-Newtonian fluids, differences in density cause variations in flow velocity during processing, which in turn affect other fluid dynamic parameters and ultimately lead to density-induced flow variations and mixing heterogeneity. The kneading block zone, being the stage of the most intensive shear mixing during extrusion, exhibits even more complex fluid flow behavior. Density variations among different carriers can lead to inadequate mixing between the carrier and the API. Neglecting such density-induced insufficient mixing may compromise the quality of the pharmaceutical product. Failure to theoretically elucidate the relationship between carrier density differences and mixing outcomes will inevitably lead to a trial-and-error approach in production process design, thereby increasing equipment debugging costs. Therefore, it is imperative to study the influence of carrier density on both fluid flow and mixing behavior to inform pre-production process design and equipment parameter optimization. This study employs FEM-based CFD simulations to model changes in flow parameters and the motion/mixing behavior of fluids within the entire kneading block zone under unidirectional extrusion forces, considering different carrier density conditions.

2 Theoretical foundation

To investigate the flow behavior of drug-carrier mixtures during HME, this project will develop a simulation model of the mixture using the Finite Element Method (FEM). The fundamental physical motions are governed by the continuity equation and the

Navier-Stokes momentum conservation equation[16,23,24]. The fluid is assumed to be incompressible, and the mixing process does not induce any net change in total volume:

$$\nabla \cdot \vec{v} = 0 \tag{1}$$

Where $\vec{v}$ is the local velocity vector of the mixture. This equation expresses the incompressibility of the fluid.

$$\rho\left(\frac{\partial \vec{v}}{\partial t} + \vec{v} \cdot \nabla \vec{v}\right) = -\nabla p + \nabla \cdot \vec{v} + \vec{f} \tag{2}$$

Where ρ is the mixture density, p is the pressure, $\vec{\tau}$ is the deviatoric stress tensor, and $\vec{f}$ is the body force (e.g., gravity). For generalized Newtonian fluids, the deviatoric stress tensor $\vec{\tau}$, which defines the non-Newtonian behavior of the fluid, is given by:

$$\vec{\tau} = 2\eta\left(\dot{\gamma}, c\right)\vec{D} \tag{3}$$

Where $\vec{D}$ is the strain rate tensor, $\dot{\gamma}$ is the shear rate, $\eta\left(\dot{\gamma}, c\right)$ is the viscosity function dependent on the shear rate $\dot{\gamma}$ and the local concentration c [25]. Given that the viscosities of both materials fall within the same order of magnitude, the shear-thinning viscosity of the mixture is computed using a linear blending rule based on the local mass fraction.

$$\vec{D} = \frac{1}{2}\left(\nabla \vec{v} + \left(\nabla \vec{v}\right)^{\mathrm{T}}\right) \tag{4}$$

$$\dot{\gamma} = \sqrt{2\vec{D} : \vec{D}} \tag{5}$$

$$\eta\left(\dot{\gamma}, c\right) = c \cdot \eta_{\mathrm{API}}\left(\dot{\gamma}\right) + \left(1 - c\right) \cdot \eta_{\mathrm{carrier}}\left(\dot{\gamma}\right) \tag{6}$$

Where η_{API} and η_{carrier} are respectively the fluid viscosities of the API and the carrier. Pharmaceutical melts generally exhibit shear-thinning behavior typical of non-Newtonian fluids, while kneading block elements generate continuously varying high

shear rates. Therefore, the Bird-Carreau model is selected to characterize rheological properties of API and carrier[22]:

$$\eta(\dot{\gamma}) = \eta_{\infty} + (\eta_0 - \eta_{\infty})\left(1 + \lambda^2 \dot{\gamma}^2\right)^{\frac{n-1}{2}} \tag{7}$$

Where $\eta(\dot{\gamma})$ is the viscosity at a given shear rate $\dot{\gamma}$, η_0 is the zero-shear viscosity of the fluid, η_{∞} is the shear viscosity at infinite shear rate, $\eta(\dot{\gamma})$ is the shear rate, λ is the time constant (often referred to as the relaxation time) associated with the fluid's characteristics, representing the response rate of the fluid's flow behavior, and n is the power-law index. The fluid exhibits shear-thinning behavior when $n < 1$, and shear-thickening when $n > 1$. The aforementioned parameters are temperature-sensitive. Since this study assumes that the melt temperature can be maintained stable at 170°C through real-time temperature control after melting, they are set as constants. The variation in shear rate induced by screw rotation is used to calculate the real-time shear viscosity in the affected region. This viscosity value is then utilized to compute the fluid motion and the shear rate for the next time step.

Since the viscosity difference between the two fluids remains within a factor of three, a unidirectional coupling approach is adopted to simplify the simulation of the flow behavior. In the mass transport calculation, the transport of the API fluid is primarily modeled by solving an additional convection-diffusion equation:

$$\frac{\partial c}{\partial t} + \vec{v} \cdot \nabla c = \nabla \cdot (D \nabla c) \tag{8}$$

Where c is the concentration of the API, t is time, $\vec{v}$ is the known velocity vector obtained from the flow field calculation, D is the molecular diffusion coefficient. In polymer melts, D typically assumes a vanishingly small value.

3 Simulation model

The kneading block zone, being the region with the most intensive mixing in the HME process, exhibits highly complex fluid flow behavior. This study employs simulation methods to model the unidirectional compressive effect on fluids via a planar interface, characterizing the extrusion action of kneading blocks, while simultaneously computing the fluid flow and mixing behavior throughout the entire kneading block section during the extrusion process. The material properties used in the simulation are listed in Table 1.In this study, F-68 is selected as the carrier material. While varying the density of F-68, all other material properties are maintained constant. Indomethacin(INM) is selected as the API material. The parameters η_0, λ and n in Equation(7) remain constants for a given material under the assumed isothermal condition. In actual production, the manufacturing line employs temperature monitoring and control to maintain the internal temperature at a fixed set point. During this process, the temperature undergoes continuous fluctuations. Since temperature variations induce changes in properties such as viscosity, this study assumes a constant temperature throughout the mixing process. To investigate the effect of carrier density, this study compares five distinct density levels of the carrier material: 980, 1,090, 1,190, 1,300, and 1,500 kg/m³.

Table 1
Material Properties.

	F-68	INM
η_0/Pa·s	1382.83	2042
λ/s	3	0.5
n	0.38	0.8

For the unidirectional fluid compression analysis, a cubic domain of 6 mm × 3 mm × 6 mm is established. The simulation of fluid under multi-directional compression is achieved by applying forces from the top and two lateral surfaces, allowing

investigation of the mechanical response and flow behavior under varied compression conditions.

For the full kneading block section, the barrel geometry is formed by the intersection of two cylinders with a center-to-center distance of 12 mm and a radius of 7 mm each, with a section lead of 15 mm. The internal co-rotating kneading blocks have a center-to-center distance of 12 mm, with a root diameter of 4.5 mm and an outer diameter of 6.5 mm. The kneading block assembly comprises five individual blocks. The two end blocks have a thickness of 2.5 mm each, while the remaining blocks are 2 mm thick. An axial inter-block gap of 1 mm is maintained, with a stagger angle of 45° between adjacent blocks, as shown in Fig. 1.

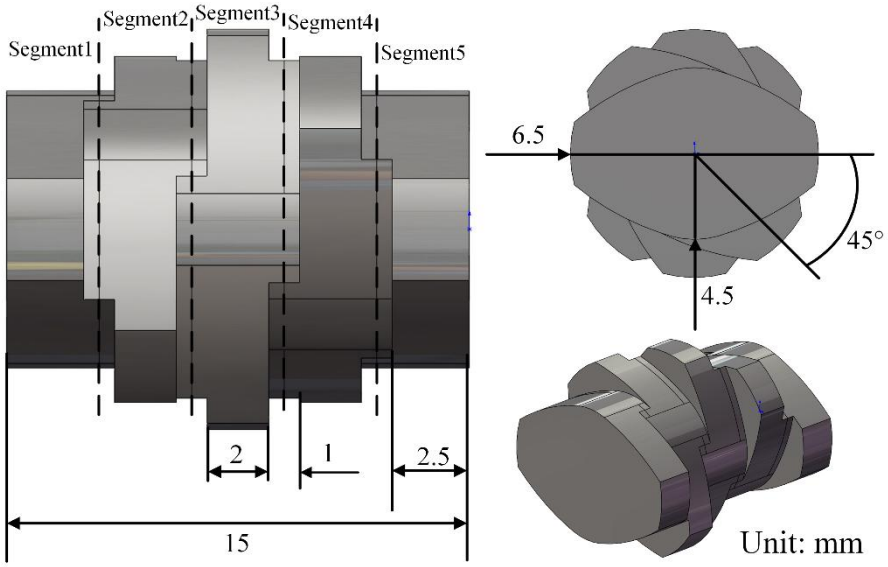


Fig. 1. Schematic Diagram and Parameters of the Twin Kneading Block Model (mm).

3.1 Transient Fluid Compression Process Model

When both API and carrier fluids are present within the domain, they exhibit relative motion during both natural flow and under compression. Due to the continuous inflow from the rear and the brief duration and unidirectional nature of the compression,

significant mixing is unlikely to occur. However, pronounced changes are observed in the flow velocities of both fluids and the morphology of their interfacial boundary.

To simulate the 6 mm × 6 mm × 3 mm subdomain subjected to kneading block compression, the initial state of the flow domain and the inlet region are set to maintain a constant velocity of 5 mm/s in the positive z-direction. The API fluid is initially located in the $x > 0$ region, and the carrier fluid occupies the $x < 0$ region. In Fig. 2 (a), the compressive surface moves downward from directly above at a velocity of 22 mm/s. The velocity of 22 mm/s represents the mean linear velocity of the individual kneading block tooth's compressive surface. The side walls and bottom surface are modeled as stationary boundaries. In Fig. 2 (b) and (c), the compression surfaces apply inward compression from the API side and carrier side respectively, while the top surface remains a fixed boundary. In all three cases, the direction of compression remains perpendicular to the fluid flow direction. In case (a), the compression surface acts simultaneously on both the API and carrier fluids, whereas in cases (b) and (c), it contacts only the API or the carrier fluid, respectively.

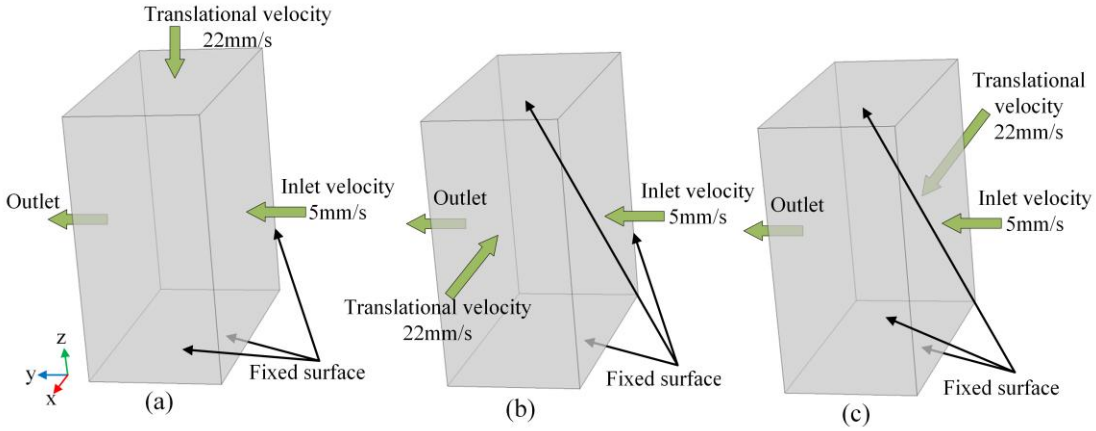


Fig. 2. Schematic of a kneading block under radial compression from different directions.

Variations in carrier density lead to divergent flow velocity responses and consequent changes in rheological properties such as viscosity. These differences in turn cause alterations in the relative motion between the two fluids, ultimately affecting

both the mixing process and its final outcome.The concentration field and interfacial boundary evolution within the flow domain are statistically analyzed to quantify the flow divergence phenomena between the two fluids following compression.

3.2 Fluid Flow and Mixing Model in the Kneading Block Zone

A flow domain model of the kneading block zone and the co-rotating twin-screw kneading blocks are established, with the two kneading blocks hereinafter referred to as Block 1 and Block 2. The temperature is maintained constant at 170°C. After setting the fluid properties, the initial feeding conditions are configured with the screw speed set to 1 r/s. The time step is defined and computed based on the duration required for a 6° rotation. The boundary and motion configurations of the flow domain are as shown in Fig. 3. After configuring the properties of the API and carrier materials, the boundary condition at Inlet 1 is set as the API inlet, while Inlet 2 is designated as the carrier inlet. To correlate with the flow variations under short-duration compression described in the first part, the API and carrier fluids are configured to enter the domain with equal volumetric flow rates, separated by the interface at x = 0.

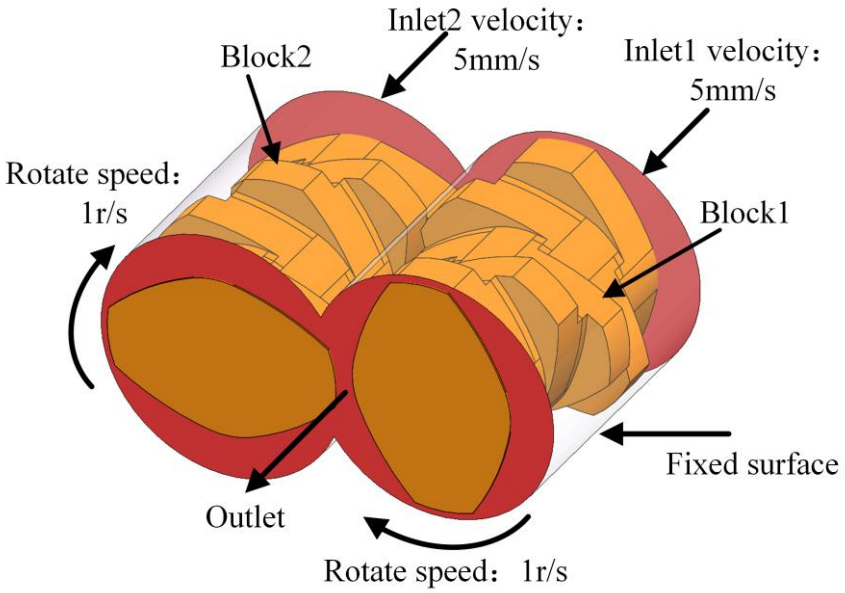


Fig. 3. Schematic of the flow field around double kneading blocks.

The fluid's flow velocity and direction are calculated from its material properties and equipment operating parameters, from which the shear rate is subsequently derived. The shear rate is used to determine the updated viscosity following shear-thinning, and this new viscosity data is subsequently fed back into the flow velocity calculation to iteratively compute the fluid motion for the next time step. The fluid flow within the kneading block section is analyzed by observing the variation in shear rate imposed by the blocks, the changes in fluid flow velocity, and the corresponding viscosity evolution during the extrusion mixing process. The step-by-step calculation procedure of the physical quantities during fluid flow is illustrated in Fig. 4.

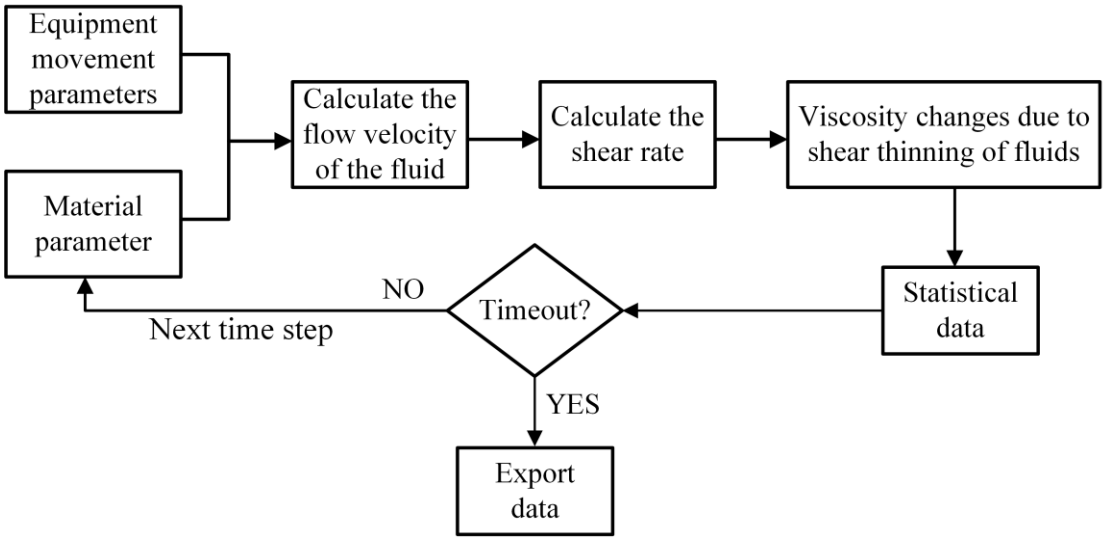


Fig. 4. A computation model for the physical quantities of fluid in the extrusion process.

For the mixing of molten fluids, the residence time and its distribution within the zone serve as key parameters characterizing both the flow behavior and mixing effectiveness. This study employs tracer particles within the simulation to characterize the transient motion of fluids in localized domains. Insufficient residence time results in inadequate mixing within this region. Conversely, excessively long residence time not only leads to overmixing, but also causes localized temperature buildup due to prolonged material retention, ultimately inducing degradation of active ingredients. The residence time distribution is calculated as follows:

$$E(t) = \frac{1}{\dot{V}} \cdot \frac{\mathrm{d}V(t)}{\mathrm{d}t} \tag{9}$$

Where $\dot{V}$ is the volumetric flow rate of the system. The mean residence time τ and the variance about the mean $\sigma_\tau^{\,2}$ can be obtained using the following formulas:

$$\tau = \int_0^\infty t\,\mathrm{E}(t)\,\mathrm{d}t \tag{10}$$

$$\sigma_\tau^{\,2} = \frac{\int_0^\infty (t-\tau)^2\,\mathrm{E}(t)\,\mathrm{d}t}{\tau^2} \tag{11}$$

The Dispersion Index[26] characterizes the deviation between the inter-particle distances of tracer particles and the ideal optimal mixing state at a given time. The deviation is quantified by comparing the actual inter-particle distances of the tracer particles with the ideal optimal inter-particle distance under perfect mixing. A smaller discrepancy indicates more effective dispersive mixing, with the deviation value being inversely proportional to the mixing performance:

$$\mathrm{DI} = \int_0^L \left| f(l) - f_{\mathrm{opl}} \right| \mathrm{d}l \tag{12}$$

Where $f(l)$ is the inter-particle distance per unit axial length, and f_{opl} is the optimal inter-particle distance per unit axial length under ideal mixing conditions.

4 Results

4.1 Transient Fluid Compression Process

Following the simultaneous compression of both fluids by the block, the fluids in different regions exhibit distinct flow behaviors. Fluid in the region adjacent to the inlet and areas distant from the compression surfaces predominantly maintains flow in the z-direction. As shown in Fig. 5, the fluid near the bottom of the inlet region exhibits a

velocity component in the positive y-direction, indicating the presence of backflow.

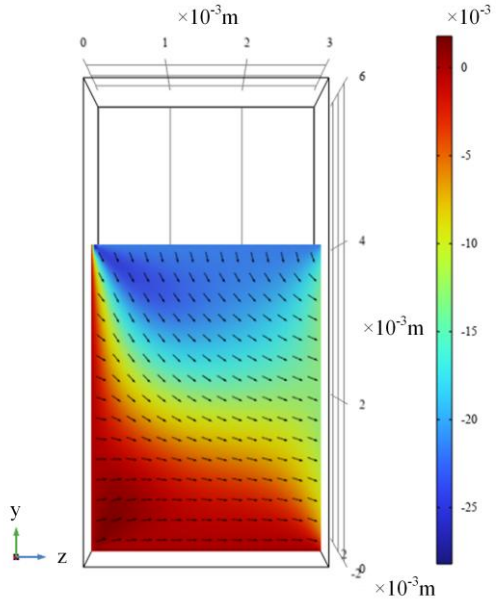


Fig. 5. Y-velocity contour and resultant velocity direction in zy-plane, on X=0 at 0.09 s.

When the kneading block simultaneously compresses both fluids in the flow domain, the differential density and the higher viscosity of the API compared to the carrier cause the API fluid to develop flow toward the carrier side. Owing to the continuous inflow of fluid and the brief duration of compression, mixing remains less pronounced in the bulk regions of both fluids, with only the concentration at the interface being significantly affected. Under unidirectional vertical compression, where shear effects are limited, both fluids exhibit minimal viscosity variation. However, owing to the higher viscosity of the API-rich fluid, the interfacial region shows a tendency for the API to migrate toward the carrier side in the central y-axis area, while the carrier moves toward the API domain in the upper and lower sections, as illustrated in Fig. 6.

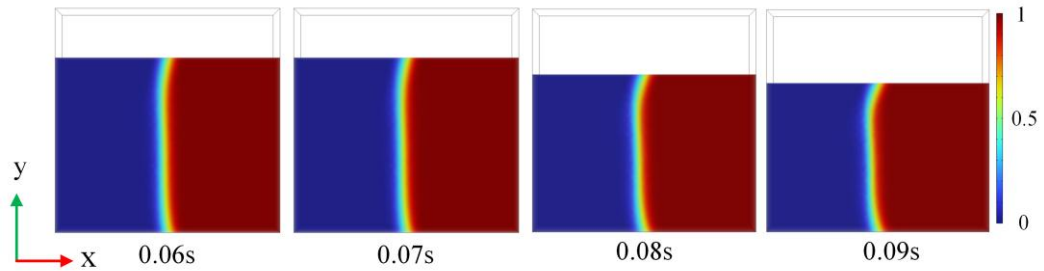


Fig. 6. Interfacial morphology and fluid distribution at the outlet during downward squeezing.

Using the 1190 kg/m³ carrier density condition as the reference, the concentration deviation along the vertical line at z = 3 mm, x = 0 mm is shown in Fig. 7. A higher carrier density results in a lower API concentration along the reference line. This implies that in the central region along the y-axis, a lower carrier density leads to increased penetration of the API-rich fluid into the carrier region.

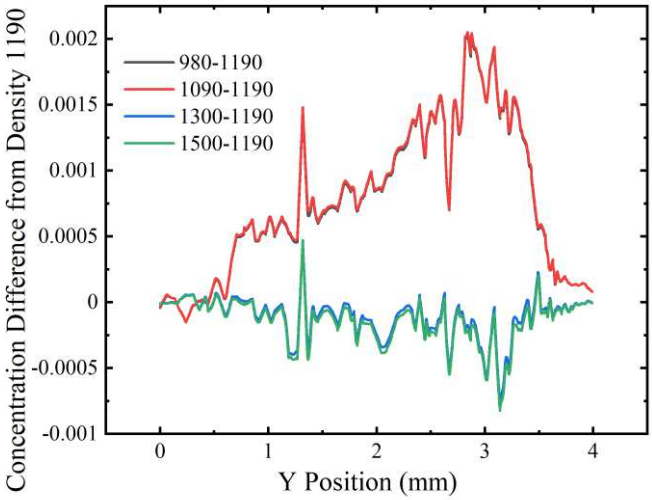


Fig. 7. API concentration difference relative to carrier density (1190) at z=3 mm, x=0 mm,t=0.09s.

Fig. 8 shows the distribution of the 0.5 concentration contour under the five carrier density conditions. Fig. 8(a) to (d) display comparative interface profiles between adjacent density conditions. The 0.5 concentration contour for the lower-density cases (980 and 1090 kg/m³), which have a greater density disparity from the API, exhibits less forward expansion but greater rear expansion compared to the higher-density cases with smaller density differences. Fluids with higher density experience more pronounced kinematic changes under block compression than those with lower density. Simultaneously, a higher carrier density results in a more pronounced settling effect due to gravity, causing increased downward migration and enhanced penetration into the API-rich region in the lower part of the rear section.

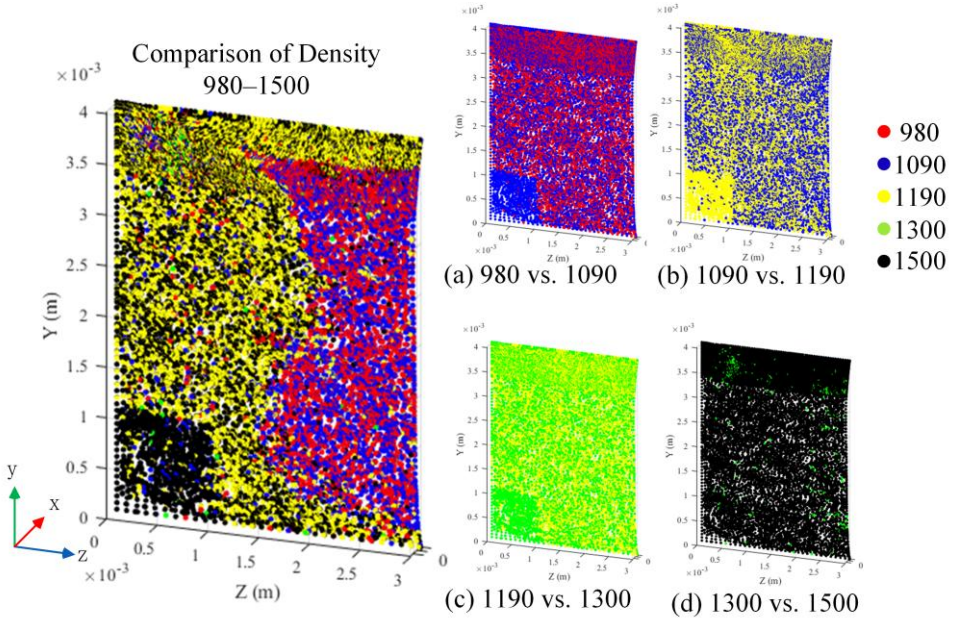


Fig. 8. The 0.5 concentration isosurface during downward squeezing for varying densities.

When the planar surface compresses the flow domain from the API side, the fluid interface exhibits a profile similar to that observed during downward compression, with the more viscous API fluid forming a pronounced convex curvature toward the carrier fluid in the central region. However, the extent of protrusion is markedly less pronounced than during downward compression, and the profile displays two subtle peaks with a slightly depressed central segment, as illustrated in Fig. 9.

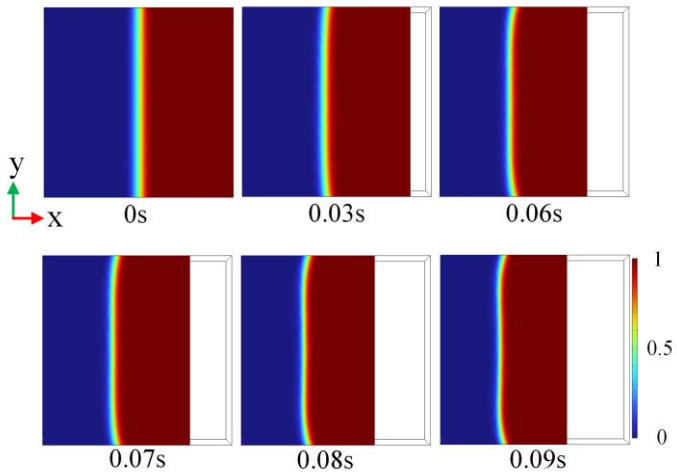


Fig. 9**.** Fluid distribution and interface at the outlet during squeezing from the API side.

When the kneading block applies compression from the API side, the pressure is initially transmitted through the API before reaching the carrier. Consequently, no

significant differences are observed across carrier density conditions under this mode of compression. The API concentration along the vertical line at z = 2.9 mm, x = -1 mm is shown in Fig. 10. The flow velocity variations exhibit minimal differences across different carrier density conditions.

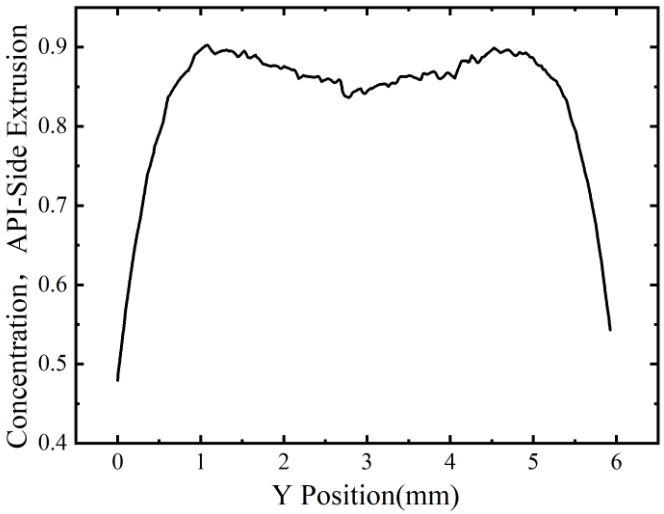


Fig. 10. API concentration on the vertical line at z=2.9 mm, x=-1 mm during squeezing from the API side.

When the kneading block compresses the flow domain from the API side, the contact interface also develops a convex curvature toward the carrier side in the central API region as it advances. The degree of interface protrusion is significantly less pronounced compared to that observed during downward compression or compression from the API side, as shown in Fig. 11 and Fig. 12.

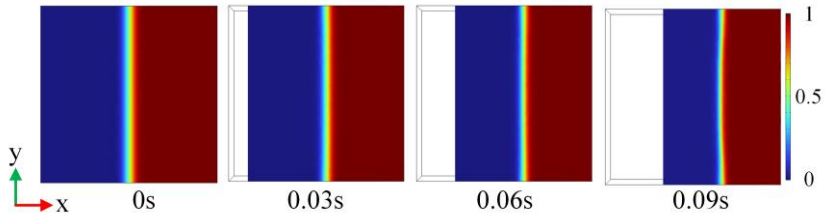


Fig. 11. Fluid distribution and interface at the outlet during squeezing from the carrier side.

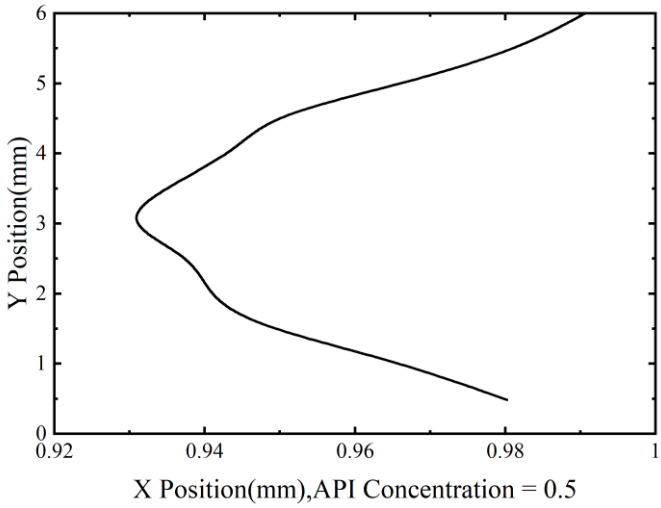


Fig. 12. The 0.5 API concentration contour at the outlet at 0.09 s during carrier-side squeezing.

The interfacial morphology between the carrier and API shows only slight variations across different carrier densities, with no significant differences observed. The concentration profile along the vertical line at z = 2.9 mm, x = 1 mm is shown in Fig. 13. When compression is applied from the carrier side, the differences in flow velocity variations among carriers of different densities remain negligible.

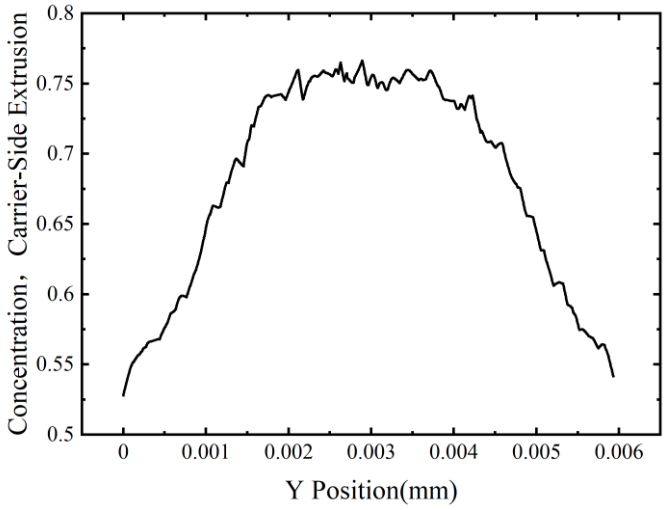


Fig. 13. API concentration on the vertical line at z=2.9 mm, x=-1 mm during squeezing from the carrier side.

When a planar surface compresses two adjacent fluids within the flow domain perpendicular to the flow direction, the initially flat interface becomes distorted. The API fluid protrudes toward the carrier side in the central zone of the interface, while the carrier fluid undergo excursion toward the API domain in the upper and lower regions.

When the planar surface compresses both fluids simultaneously or acts exclusively on the API fluid, the interfacial excursion becomes more pronounced. The effect of carrier density difference on fluid excursion remains minimal when the compression surface is in contact with only one fluid phase. When both fluids undergo compression simultaneously, the API fluid demonstrates marked excursion toward the carrier fluid. At the same time, differences in both compressive thrust and shear-thinning response under varying carrier densities lead to a progressive increase in the extent of this excursion as the carrier density decreases.

4.2 Fluid Flow Parameters in Different Regions of the Kneading Block Section

During the mixing process, the fluid undergoes compression by the kneading blocks, which primarily provide radial compression with minimal axial conveying force. Under these conditions, mixing occurs primarily through shear-driven mechanisms. The axial transport of fluid within this zone is largely derived from the conveying action generated in the flighted screw sections upstream and downstream of the kneading block. The shear stress exerted by the kneading blocks on the fluid is converted into changes in flow velocity, which in turn alters the shear rate. As a result, fluids with different carriers undergo variations in both hydrodynamic parameters and material properties during the extrusion mixing process.

In co-rotating twin-screw extruders, the flow behavior is not kinematically symmetric between the two sides. Thus, nine characteristic points (P1–P9) are sampled within the same cross-section, as shown in Fig. 14. Axially, the kneading block is divided into five segments, as shown in Fig. 1.

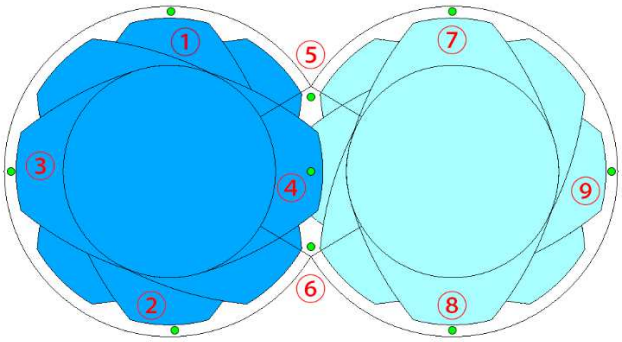


Fig. 14. On a cross-section: selected characteristic points.

The coordinates of the feature points are listed in Table 2. Points 3 and 9, situated in the outermost areas of the cross-section, experience compression almost exclusively from a single kneading block, closely resembling the conditions observed in single-block extrusion. Points 1, 2, 7, and 8 are influenced by the opposite kneading block, though to a limited extent. Points 4, 5, and 6 lie within the intermeshing region and are simultaneously subjected to compressive forces from both kneading blocks.

Table 2
Coordinates of the selected feature points.

	X(mm)	Y(mm)
Point1	6	6.7
Point2	6	-6.7
Point3	12.7	0
Point4	0	0
Point5	0	3
Point6	0	3
Point7	-6	6.7
Point8	-6	-6.7
Point9	-12.7	0

In the narrow zones outside the kneading region, the fluid is influenced by only a single kneading block, and its motion closely resembles that in a single-screw extrusion environment. The selection of these characteristic zones is illustrated in Fig. 15. The three connected surfaces are unwrapped into a single plane to better visualize the shear rate distribution along the periphery. The influence of the kneading blocks on the fluid, as it varies along the kneading block zone, is shown in Fig. 16 and Fig. 17. The region experiencing the highest shear from a single kneading block is located at the tip area,

with the peak value of 105.47 s^{-1} occurring at the junction between the tip and flank.

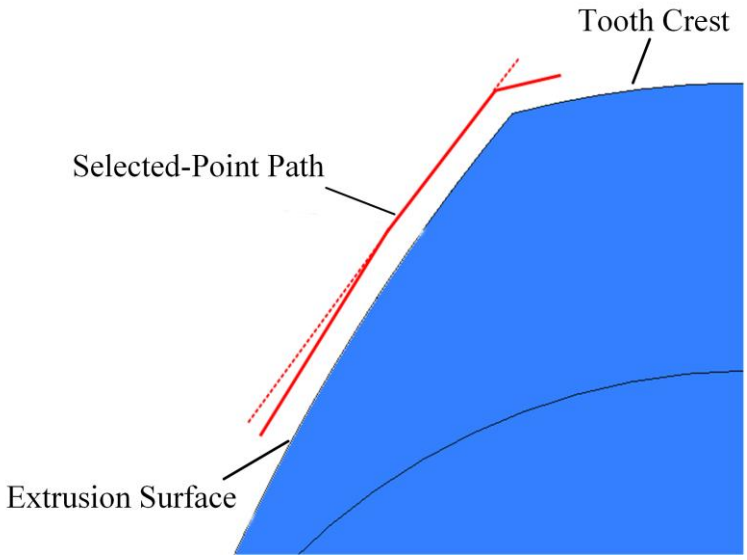


Fig. 15. Region selection from tooth tip to root.

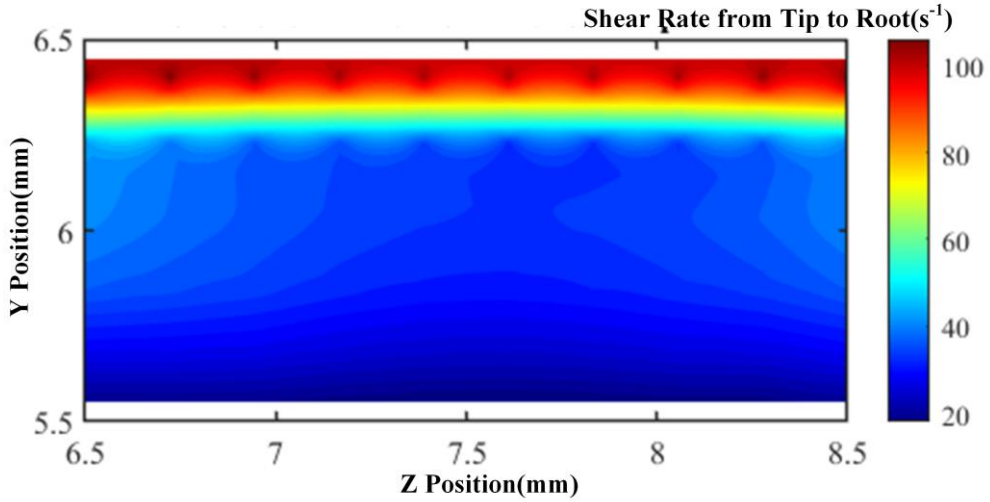


Fig. 16. Shear rate effect on fluid from different zones of a single kneading block in a narrow peripheral region.

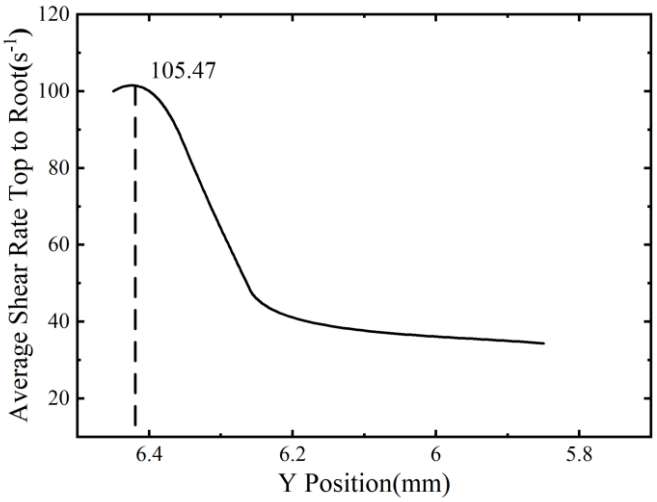


Fig. 17. Variation of shear rate from tooth tip to root.

In the intermeshing region, the two co-rotating kneading blocks move in opposite directions relative to the material: Block 1 shears the fluid upward through the region, while Block 2 shears it downward. As shown in Fig. 18, before the kneading blocks enter the intermeshing zone, the relatively open geometry in this region results in low shear rates, while the highly confined spaces near the tip areas of both blocks produce significantly higher shear rates. To highlight the distinct shear characteristics across different regions, different scale ranges are applied at different time points during the analysis. As shown in Fig. 18 (a)–(e), between 0.1 s and 0.117 s, Block 1 is about to enter the intermeshing zone while Block 2 does not fully exit. The region of maximum shear rate is located near the trailing tip of Block 2. As shown in Fig. 18 (h)–(i), from 0.134 s to 0.2 s, Block 2 has just exited the intermeshing zone and no longer contributes significant shear, but still causes flow obstruction. During this period, the maximum shear shifts to the leading tip of Block 1. As Block 2 moves farther from the intermeshing zone, the increased flow area results in reduced shear rates.

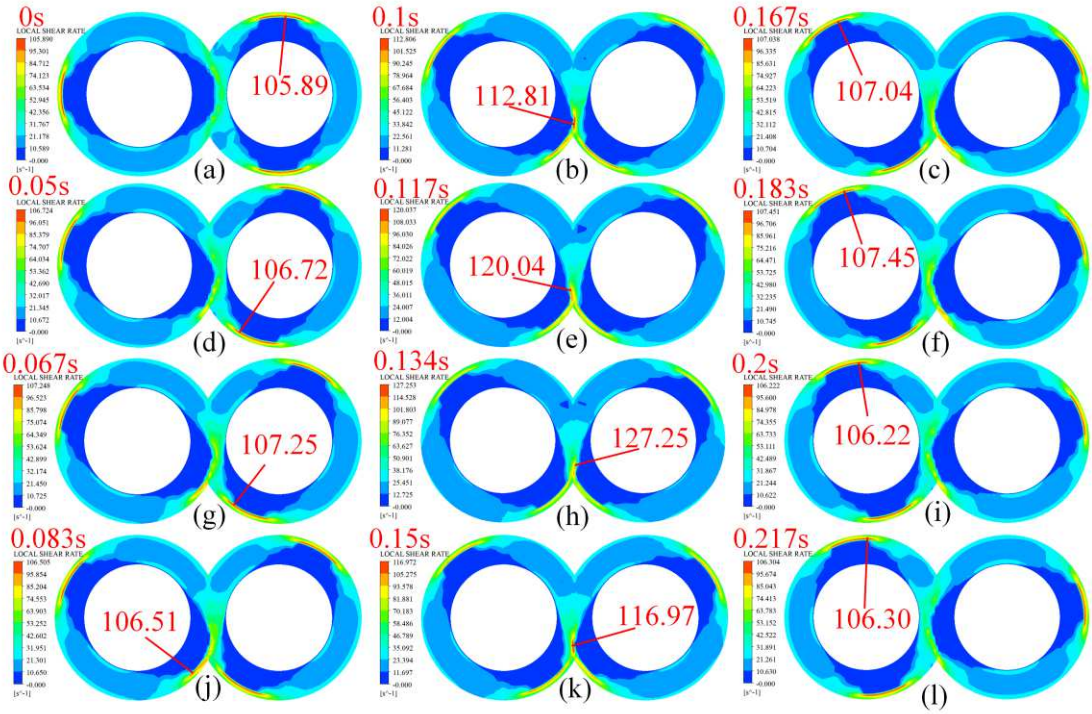


Fig. 18. Shear rate contours and peak parameters in the kneading block region from 0.05 s to 0.217 s.

Points 3 and 9 experience minimal influence from the opposite kneading block and are primarily affected by a single block. The shear rate and other relevant parameters in the regions of Points 3 and 9 are shown in Fig. 19. In the compressed zone, the shear rate rises sharply relative to other areas, accompanied by increased flow velocity. Fluid viscosity decreases as the shear rate rises. The peak shear rate is located at the periphery of the block, while the block tip exhibits a slight depression. Regions that have just been exited by the block or are about to be engaged experience minimal compression. At the minimum root diameter of the block, compression is almost negligible, and this area represents the largest cross-section in the barrel. Shear-driven mixing is therefore weak here, and the fluid motion is dominated more by the conveying action from upstream, resulting in a higher velocity component in the z-direction. Meanwhile, the kneading block passes through the tip region at both ends of the section corresponding to Point 9, while its root section aligns with the central portion. This results in a flow pattern that is nearly the converse of that observed in the corresponding

region of Point 3.

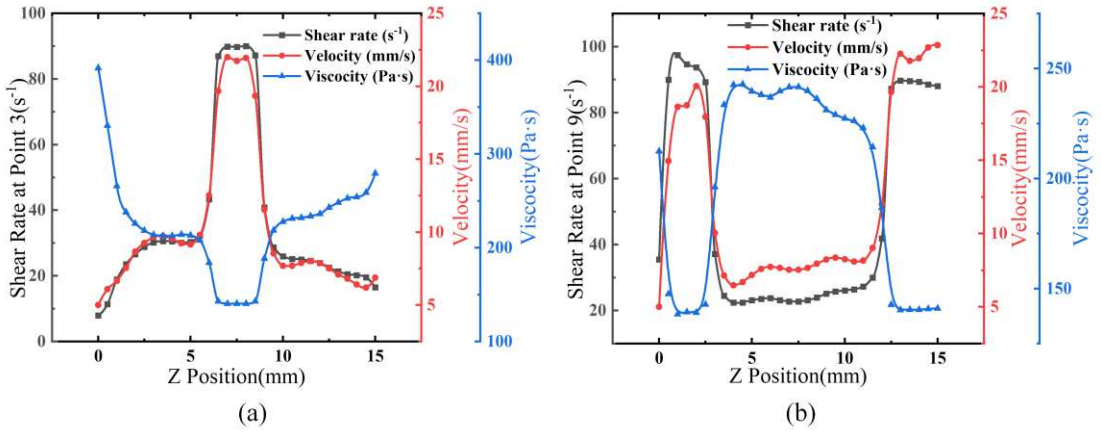


Fig. 19. Shear rate, velocity, and viscosity along the segment between points 3 and 9.

Points 1, 2, 7, and 8, although closer to the intermeshing region than Points 3 and 9, remain under the direct influence of only a single kneading block. The shear rate and related parameters at Points 1 and 8 are shown in Fig. 20. At 2.5 s, Points 3 and 8, as well as Points 1 and 9, exhibit identical kneading block geometric profiles. The overall variation in parameters such as shear rate follows nearly identical trends.

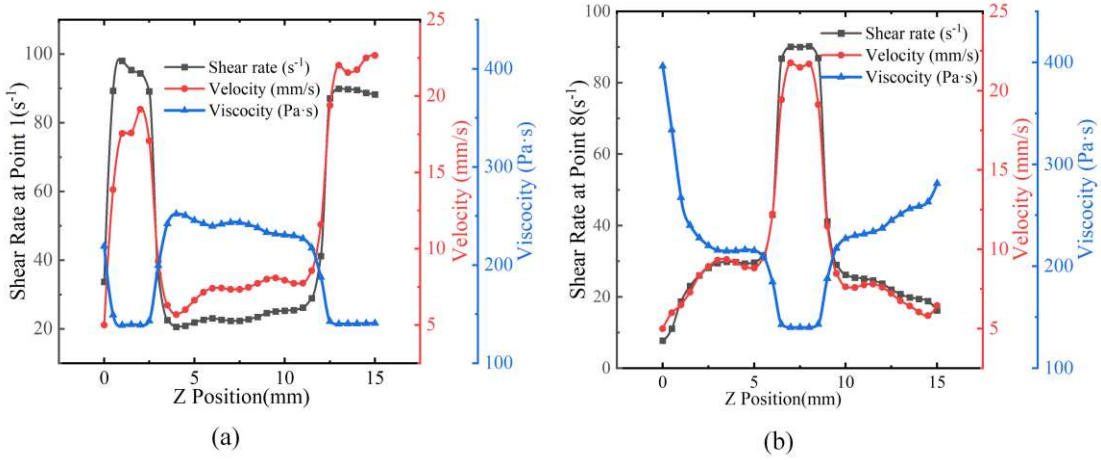


Fig. 20. Shear rate, velocity, and viscosity along the segment between points 1 and 8.

Points 4, 5, and 6 lie within the engagement zone and are simultaneously subjected to the engagement of both kneading blocks. Their shear rate and related parameters are shown in Fig. 21. At Point 4, Segment 3 is fully covered by the kneading block, while Segment 2 is under compression and Segment 4 is in a disengaged state. The shear rate decreases gradually from the block tip toward the

inter-flank gap, and the viscosity is inversely proportional to both the shear rate and the flow velocity. At 0.25 s, Point 5 is located near z = 0 and z = 10.5 mm where both kneading blocks are moving away from it, resulting in minimal compression and a low shear rate. In the vicinity of z = 4.5 mm, the right screw has moved away from this zone, while the left kneading block continues to apply compression to the fluid in this region, causing the shear rate to sharply increase.

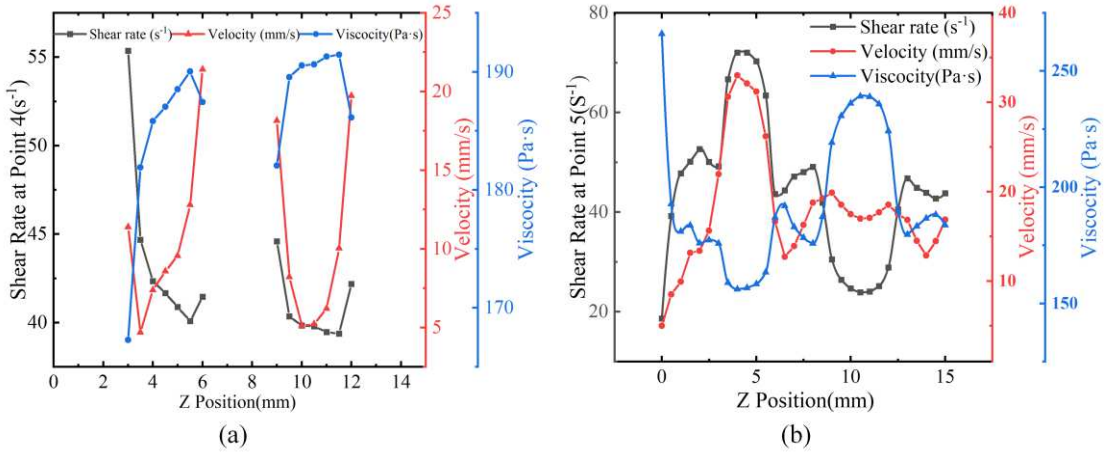


Fig. 21. Shear rate, velocity, and viscosity along the segment between points 4 and 5.

4.3 Fluid Flow in the Kneading Block Section: Time-Dependent Behavior

Points 3 and 9 in the outermost regions experience minimal influence from the opposite kneading block and are predominantly affected by a single block. Their shear rate variations are shown in Fig. 22. At 0.05 s, Point 3 in the 0–2.5 mm axial segment lies in the trailing tip region of the block, where the shear rate remains high. Meanwhile, the block begins to approach the vicinity of Point 3 in the 3.5–5.5 mm segment, causing the shear rate to rise. Due to the 1 mm axial gap between adjacent blocks, this region is influenced by both blocks but without direct compression, leading to the observed decrease in shear rate at the 3 mm position.

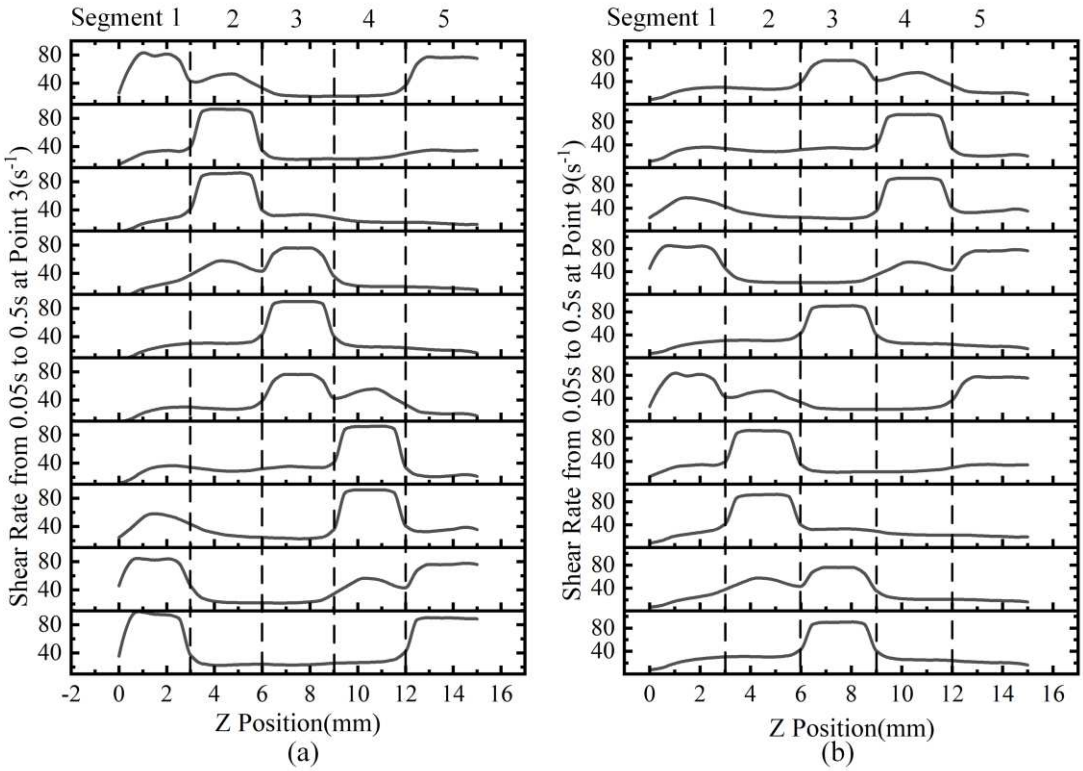
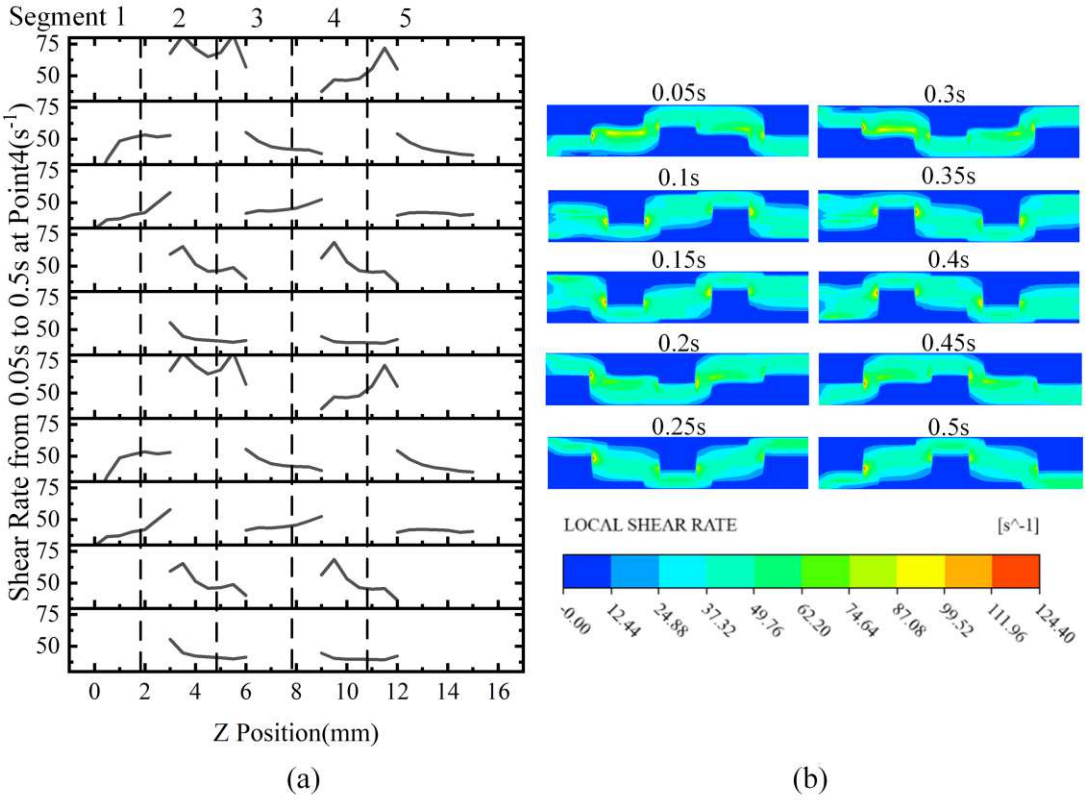


Fig. 22. Shear rate variation over time at points 3 and 9.

Points 4, 5, and 6 are located within the engagement zone and simultaneously subjected to the engagement of both kneading blocks. Their shear rate variations are shown in Fig. 23 and Fig. 24. At 0.05 s, Segments 1, 3, and 5 are fully engaged by kneading blocks covering the central axis including portions of Point 4. During this phase, Segment 2 is compressed by the right screw in a top-to-bottom direction, while Segment 5 is compressed by the left screw in a bottom-to-top direction. At 0.1 s, Segments 2 and 5 are engaged over the central axis while the left shaft Segments 1, 5 and right shaft Segment 3 had disengaged from the zone. Meanwhile, the left shaft Segment 3 and right shaft Segments 1, 5 had not yet entered the region. The peak shear rates are observed at Points 5 and 6, while the shear rate in the Point 4 region remained relatively low. During single-block engagement with significant shear effects. the shear action is predominantly concentrated in the peripheral regions of the block, while the central zone experiences a moderate decrease in shear rate.



(a) (b)

Fig. 23. Shear rate variation over time at points 4.

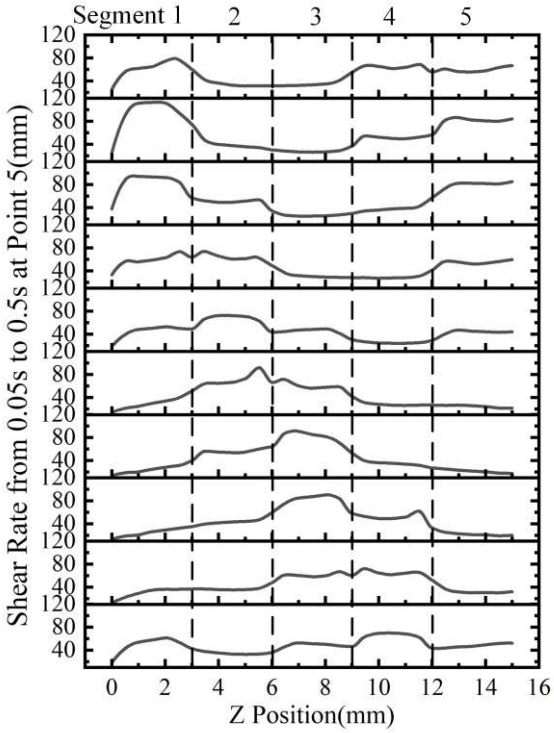


Fig. 24. Shear rate variation over time at points 5.

As shown in Fig. 25, variations in carrier density alter the fluid motion induced by kneading blocks. In narrow zones subjected to single-block compression, higher carrier

density produces more pronounced flow velocity variations. This effect accumulates along the flow direction from the inlet to the outlet with prolonged exposure to shear forces.

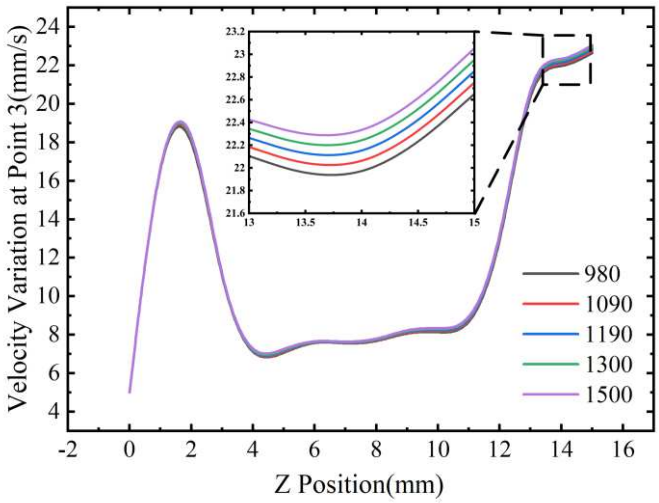


Fig. 25. Velocity variation at point 3 for carriers with different densities.

In the engagement zone, subjection to shear from both kneading blocks results in highly complex fluid flow patterns, as shown in Fig. 26. Fluids with higher density exhibit greater flow velocity variation under kneading block compression, demonstrating faster acceleration and higher peak velocity values after compression. Meanwhile, as the kneading blocks disengage, the flow velocity declines more rapidly for denser fluids. The difference in minimum velocity values across fluids is smaller than the difference in their peak values and remains less distinct, with cases observed where the fluid with the lowest value may vary among different carrier densities.

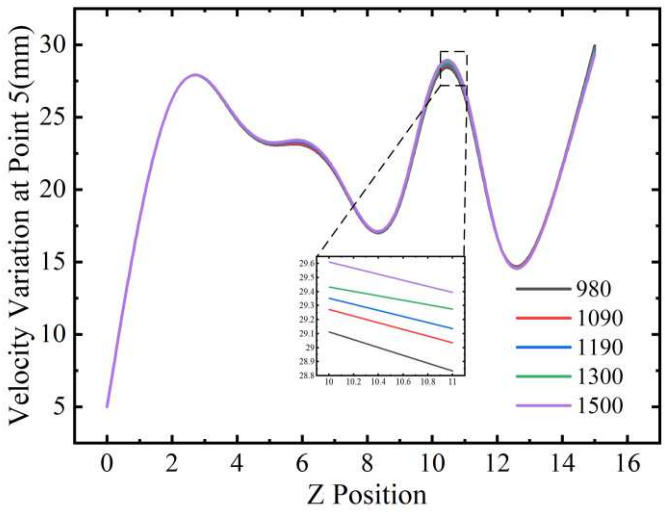


Fig. 26. Velocity variation at point 5 for carriers with different densities.

4.4 Fluid Mixing in the Kneading Block Zone

Residence time refers to the duration required for a fluid element to travel from the inlet to the outlet of a defined region, while the Residence Time Distribution (RTD) characterizes the statistical variation in these residence times among different fluid elements. A wide variation in residence time among fluid elements within the same flow domain indicates that some portions of the fluid experience either insufficient residence or prolonged retention. This results in non-uniform mixing.

The axial (z-direction) flow velocity in different regions of the domain is a critical parameter influencing the residence time. The z-direction velocity profile within Segment 3 of the kneading block is shown in Fig. 27. In addition to backflow caused by the resistance from forward fluid compression, the mixing process within the kneading block section exhibits distinct reverse flow near the block tips due to the alternating compression and disengagement of the kneading blocks. When the block tip compresses the regional fluid, the fluid at higher z-coordinates accelerates forward, while the fluid at lower z-coordinates develops reverse flow. Conversely, as the block disengages from the region, fluid at higher z-coordinates develops reverse flow, while

fluid at lower z-coordinates accelerates in the forward direction.

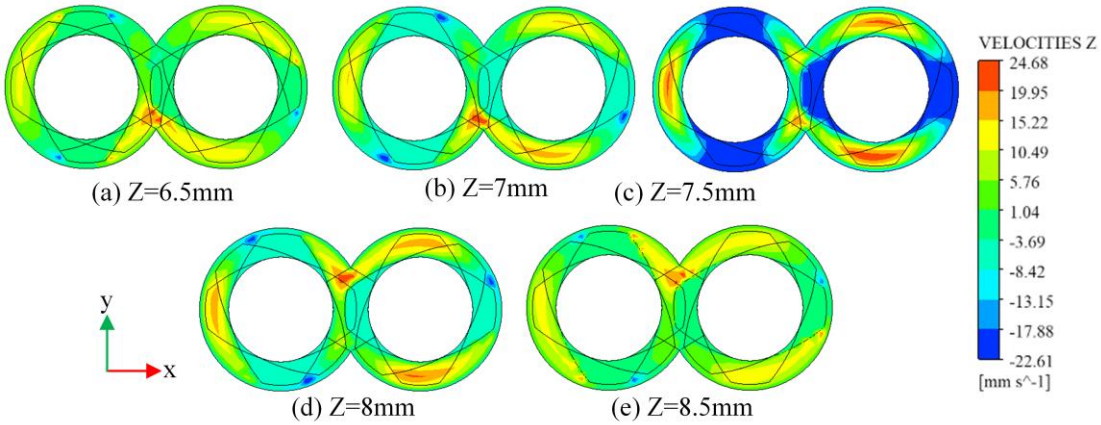


Fig. 27. Z-velocity contours at six equally-spaced sections (z=0.65-0.85).

The RTD curves for carrier fluids of different densities are shown in Fig. 28. The RTD curves exhibit a bimodal profile, with a secondary peak at approximately 2 s and the primary peak occurring at around 2.5 s. A secondary portion of the fluid exits the domain between 1.7 s and 2 s, while the main body leaves around 2.5 s. The relatively small fraction exiting at other times indicates that these two periods represent the dominant flow patterns. Pronounced backmixing is evidenced within the kneading block section of the HME process. During the earlier secondary peak, fluids with different carrier densities exit the flow domain quickly and experience minimal repeated compression, thus exhibiting negligible variation. At the peak of the residence time, however, the prolonged interaction with the kneading blocks leads to discernible differences among fluids with varying carrier densities. As the carrier density increases, the peak residence time decreases. This suggests that after sufficient kneading block compression, higher carrier density leads to shorter fluid residence time in the zone.

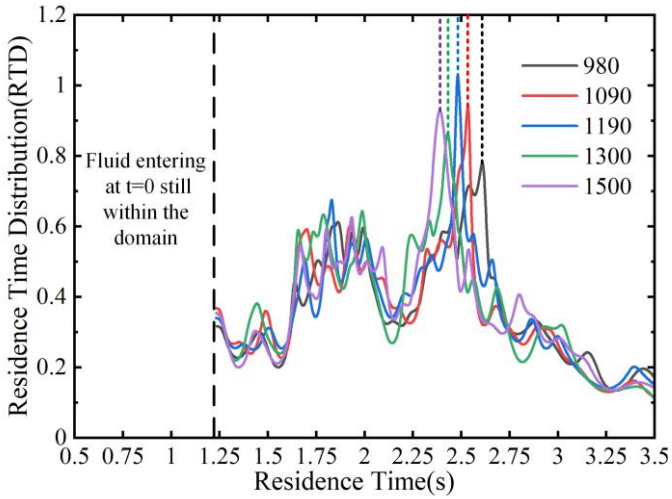


Fig. 28. Residence time distribution of carrier fluids with different densities.

The Dispersion Index (DI) serves as an effective metric for quantifying the performance of mixing processes. Consider a mixing process within a closed system where, at the initial moment, a small number of tracer particles are concentrated in a localized region, forming a high-concentration agglomerate. As the process evolves under the action of the flow field, the particles representing the fluid gradually disperse, and their spatial distribution changes over time. To evaluate the deviation between the instantaneous distribution and the ideal homogeneous state, the spatial distance distribution function of tracer particles can be applied. The degree of discrepancy between the current distribution and the optimal uniform distribution is quantified: a larger deviation indicates poorer system homogeneity, while a smaller value signifies a closer approach to the uniform state and thus better mixing performance.

The temporal evolution of the inter-particle distance distribution for the tracer particles under the carrier density condition of 1190 kg/m³ is shown in Fig. 29. At the initial stage, the particles are set to enter the flow domain simultaneously in an idealized configuration with uniform inter-particle spacing, resulting in a highly concentrated distance distribution. After a period of mixing, the particles follow highly divergent trajectories due to the mixing action, leading to variations in inter-particle distances.

After a certain duration, although the system continues to evolve, the magnitude of variation in inter-particle distances significantly diminishes.

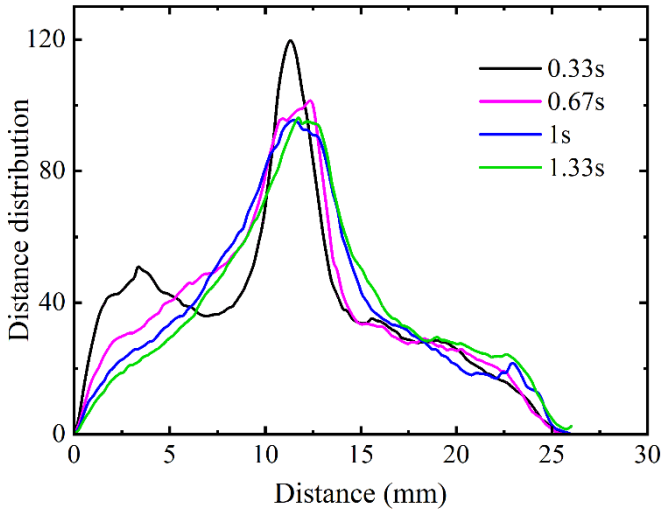


Fig. 29. Time evolution of the distance distribution of tracer particles during mixing.

The Dispersion Index under different carrier density conditions is shown in Fig. 30. The fluid is initialized as separated and uniformly distributed upon entering the domain, leading to a sharp increase in the Dispersion Index during the initial mixing phase. This initial rise is followed by a subsequent fluctuating decline. Fluids with higher carrier density are subjected to more pronounced mechanical stress, resulting in greater flow velocity variations and a more rapid increase in the Dispersion Index during the initial phase compared to lower-density fluids. Fluids with lower density consistently exhibit a lower Dispersion Index than those with higher density at the same time points. Throughout the process, the decrease in the Dispersion Index varies with carrier density. However, in the later stages, the index is influenced more significantly by the density difference between the carrier and the API. Systems with a smaller density difference attain a lower Dispersion Index compared to those with a larger density difference.

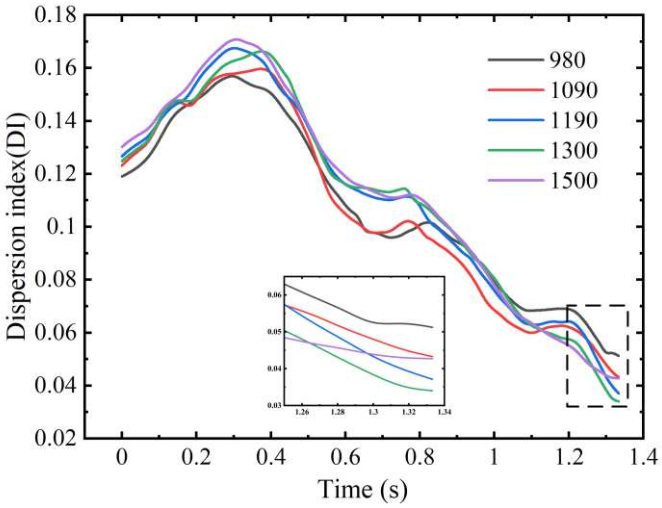


Fig. 30. Dispersion Index of fluid in different density environments.

5 Discussion

HME technology has seen well-established research and application in fields such as the plastics industry, and its adoption in the pharmaceutical sector has already laid a preliminary foundation. Parameters such as screw speed, screw configuration, and feed rate—along with their effects on mixing—have been studied extensively, with well-documented conclusions. Tianwen Dong et al. [20] simulated the flow and mixing behavior of high-viscosity fluids in conveying elements of twin-screw extruders using a parallelized smoothed particle hydrodynamics (SPH) method, assuming constant viscosity. In contrast, this study incorporates the shear rate and real-time viscosity of fluids in pharmaceutical HME by solving the Navier-Stokes equations, treating viscosity as a dynamic variable dependent on flow conditions to compute the fluid flow and mixing process within the kneading block section. Song et al. [17] introduced the concept of overlap concentration through comparative analysis of viscosity characteristics to assess the physical stability of amorphous solid dispersions (ASDs), whereas this work aims to investigate the influence of carrier density variations—a distinct physical property—on the mixing process and its outcome.

When subjected to compression, the high viscosity ratio between the API and the carrier results in relatively stable flow behavior with limited lateral penetration, which aligns with the interfacial evolution between two abruptly contacted fluids described by Redapangu et al. [27]. Under different contact conditions of the compression surface with the fluids, distinct interfacial morphologies develop, manifesting as varying degrees of excursion of the higher-viscosity API fluid toward the carrier side. The carrier density also influences this excursion behavior. This phenomenon thereby leads to variations in the mixing process along the kneading block section under different carrier density conditions. Higher carrier density induces more pronounced flow velocity variations and accelerates dispersion and mixing efficiency. However, under otherwise constant parameters and after sufficient mixing, carriers with a smaller density difference from the API fluid achieve a superior mixing outcome.

This study is based on the industrial practice of temperature control, assuming a constant temperature throughout the process. However, it is recognized that extrusion and shear inherently generate heat, leading to temperature-dependent variations in material properties such as viscosity. Subsequent studies should further address the influence of these temperature variations during extrusion. To model the mixing process, the boundary setup initializes the two fluids in a simple side-by-side configuration entering at uniform velocity, thereby neglecting pre-mixing and flow variations from upstream flighted screw sections. A multi-domain coupled simulation approach is required to refine the computational accuracy.

6 Conclusion

This study investigates the flow and mixing behavior of molten drug-carrier blends within the kneading block section during pharmaceutical HME. The results demonstrate

that variations in carrier density during HME lead to changes in fluid flow, inducing distinct excursion phenomena that consequently affect both the mixing process and its outcome. The main conclusions are as follows:

(1) Under unidirectional compression, fluids moving in the same flow direction develop distinct excursion patterns depending on which fluid phase is contacted by the compression surface. When both fluids are subjected to compression, differences in carrier density result in a more pronounced excursion of the API fluid toward the carrier side under higher carrier density conditions.

(2) During the process where kneading block compression induces changes in fluid parameters, the shear rate is directly proportional to the flow velocity variation and inversely proportional to the viscosity. The primary location where the kneading block induces variations in fluid shear rate is radially situated at the junction between the tip edge and the flank surface. Axially, the shear effect in the central plane is marginally lower than that at the peripheral edges.

(3) The alternating compression and disengagement by the kneading blocks induce localized fluid acceleration or backflow, which increases the complexity of fluid passage through the mixing zone. In terms of residence time, a higher carrier density leads to a shorter residence time, thereby influencing the mixing outcome.

(4) During the extrusion process, the homogeneity of the two-fluid mixture first decreases and then undergoes a fluctuating increase. Fluids with higher carrier density exhibit steeper rates of both the initial decline and the subsequent fluctuation. However, after sufficient mixing, the resulting homogeneity depends more strongly on the density difference between the carrier and the drug. A smaller density difference leads to a more uniform final mixture.

CRediT authorship contribution statement

Qi Shen: Writing - Editing Formal analysis Writing- Original draft preparation. **Yibiao Chen**: Conceptualization, Methodology, Software, Funding acquisition. **Huagui Li**: Data curation. **Wutong Wu**: Resources, Project administration. **Hongming Zhou**: Writing – Review.

Declaration of Competing Interest

The authors declare that they have no known competing financial interests or personal relationships that could have appeared to influence the work reported in this paper.

Acknowledgements

The authors acknowledge the support of the National Natural Science Foundation of China (Grant No. 52505209) and the key Science, Technology Innovation Project of Wenzhou (Grant No. ZY2023011, No. ZG2023004, No. zL20250043).

References

[1] S. Bandari, D. Nyavanandi, V.R. Kallakunta, K.Y. Janga, S. Sarabu, A. Butreddy, M.A. Repka, Continuous twin screw granulation – An advanced alternative granulation technology for use in the pharmaceutical industry, International Journal of Pharmaceutics 580 (2020) 119215. https://doi.org/10.1016/j.ijpharm.2020.119215.

[2] J. Matić, A. Paudel, H. Bauer, R.A.L. Garcia, K. Biedrzycka, J.G. Khinast, Developing HME-Based Drug Products Using Emerging Science: a Fast-Track Roadmap from Concept to Clinical Batch, AAPS PharmSciTech 21 (2020) 176. https://doi.org/10.1208/s12249-020-01713-0.

[3] J.E. Martínez-Jiménez, I. Sathisaran, F. Reyes Figueroa, S. Reyes, M. López-Nieves, C.P. Vlaar, J.-C.M. Monbaliu, R. Romañach, G. Ruaño, T. Stelzer, J. Duconge, A review of precision medicine in developing pharmaceutical products: Perspectives and opportunities, International Journal of Pharmaceutics 670 (2025) 125070. https://doi.org/10.1016/j.ijpharm.2024.125070.

[4] A. Eitzlmayr, G. Koscher, G. Reynolds, Z. Huang, J. Booth, P. Shering, J. Khinast, Mechanistic modeling of modular co-rotating twin-screw extruders, Int. J. Pharm. 474 (2014) 157–176. https://doi.org/10.1016/j.ijpharm.2014.08.005.

[5] X. Li, X. Hong, S. Shuai, X. Han, C. Li, H. Zhang, Z. Wang, M. Ren, L. Jin, A. Zheng, A review of hot melt extrusion technology: Advantages, applications, key factors and future prospects, Journal of Drug Delivery Science and Technology 98 (2024) 105884. https://doi.org/10.1016/j.jddst.2024.105884.
[6] H. Patil, S.K. Vemula, S. Narala, P. Lakkala, S.R. Munnangi, N. Narala, M.O. Jara, R.O. Williams III, H. Terefe, M.A. Repka, Hot-Melt Extrusion: from Theory to Application in Pharmaceutical Formulation-Where Are We Now?, AAPS PharmSciTech 25 (2024) 37. https://doi.org/10.1208/s12249-024-02749-2.
[7] Y. Ren, L. Mei, L. Zhou, G. Guo, Recent Perspectives in Hot Melt Extrusion-Based Polymeric Formulations for Drug Delivery: Applications and Innovations, AAPS PharmSciTech 20 (2019) 92. https://doi.org/10.1208/s12249-019-1300-8.
[8] S.P. Forster, E. Dippold, T. Chiang, Twin-Screw Melt Granulation for Oral Solid Pharmaceutical Products, Pharmaceutics 13 (2021) 665. https://doi.org/10.3390/pharmaceutics13050665.
[9] J. Han, M. Tang, Y. Yang, W. Sun, Z. Yue, Y. Zhang, Y. Zhu, X. Liu, J. Wang, Amorphous solid dispersions: Stability mechanism, design strategy and key production technique of hot melt extrusion, International Journal of Pharmaceutics 646 (2023) 123490. https://doi.org/10.1016/j.ijpharm.2023.123490.
[10] M. Monschke, K. Kayser, K.G. Wagner, Processing of Polyvinyl Acetate Phthalate in Hot-Melt Extrusion-Preparation of Amorphous Solid Dispersions, Pharmaceutics 12 (2020) 337. https://doi.org/10.3390/pharmaceutics12040337.
[11] A. Ren, J.E. Spahn, H.D.C. Smyth, F. Zhang, Twin-screw continuous mixing: Effect of mixing elements and processing parameters on properties of aerosol powders, Powder Technology 424 (2023) 118519. https://doi.org/10.1016/j.powtec.2023.118519.
[12] M. Hanada, S.V. Jermain, X. Lu, Y. Su, R.O. Williams, Predicting physical stability of ternary amorphous solid dispersions using specific mechanical energy in a hot melt extrusion process, International Journal of Pharmaceutics 548 (2018) 571–585. https://doi.org/10.1016/j.ijpharm.2018.07.029.
[13] R.M. Dhenge, Twin screw wet granulation: Effect of powder feed rate, Advanced Powder Technology (2011).
[14] P. Srinivasan, M. Almutairi, A.A.A. Youssef, A. Almotairy, S. Bandari, M.A. Repka, Numerical simulation of five different screw configurations used during the preparation of hot-melt extruded Kollidon® and Soluplus® based amorphous solid dispersions containing indomethacin, Journal of Drug Delivery Science and Technology 85 (2023) 104561. https://doi.org/10.1016/j.jddst.2023.104561.
[15] A. Pradhan, B. Phillips, F. Yang, K. Karan, T. Durig, B. Haight, C. Martin, F. Zhang, Optimizing twin-screw melt granulation: The role of overflight clearance on granulation behavior, International Journal of Pharmaceutics 653 (2024) 123900. https://doi.org/10.1016/j.ijpharm.2024.123900.
[16] C.O. Ufodike, G.C. Nzebuka, Investigation of thermal evolution and fluid flow in the hot-end of a material extrusion 3D Printer using melting model, Additive Manufacturing 49 (2022) 102502. https://doi.org/10.1016/j.addma.2021.102502.
[17] S. Song, C. Wang, B. Zhang, C.C. Sun, T.P. Lodge, R.A. Siegel, A Rheological Approach for Predicting Physical Stability of Amorphous Solid Dispersions, J. Pharm. Sci. 112 (2023) 204–212. https://doi.org/10.1016/j.xphs.2022.08.028.
[18] W. Qin, S. Li, H. Bai, S. Jia, Structural design and heat transfer analysis of twin-screw extrusion 3D printer, Int. J. Adv. Manuf. Technol. 130 (2024) 5601–5618. https://doi.org/10.1007/s00170-024-13010-2.
[19] H. Suwardie, P. Wang, D.B. Todd, V. Panchal, M. Yang, C.G. Gogos, Rheological study of the mixture of acetaminophen and polyethylene oxide for hot-melt extrusion application, European Journal of Pharmaceutics and Biopharmaceutics 78 (2011) 506–512. https://doi.org/10.1016/j.ejpb.2011.03.013.
[20] T. Dong, S. Jiang, J. Wu, H. Liu, Y. He, Simulation of flow and mixing for highly viscous fluid in a twin screw extruder with a conveying element using parallelized smoothed particle hydrodynamics, Chemical Engineering Science 212 (2020) 115311. https://doi.org/10.1016/j.ces.2019.115311.
[21] B. Lang, J.W. McGinity, R.O. Williams, Hot-melt extrusion – basic principles and

pharmaceutical applications, Drug Development and Industrial Pharmacy 40 (2014) 1133–1155. https://doi.org/10.3109/03639045.2013.838577.
[22] K. Yoon, H.W. Jung, M.-S. Chun, Secondary Dean flow characteristics of inelastic Bird-Carreau fluids in curved microchannels, Korea-Aust. Rheol. J. 32 (2020) 61–70. https://doi.org/10.1007/s13367-020-0007-4.
[23] T. Chang, B.J. Jin, Global well-posedness of the Navier-Stokes equations of an inhomogeneous fluid in the half-space with inflow boundary condition, Journal of Mathematical Analysis and Applications 482 (2020) 123567. https://doi.org/10.1016/j.jmaa.2019.123567.
[24] H. Chen, Z. Chen, X. Wang, X. Yi, X. Zhang, Z. Luo, Mass transfer and bubble hydrodynamics in stirred tank with multiple properties fluid via a CFD-PBM method, Can J Chem Eng 102 (2024) 4038–4054. https://doi.org/10.1002/cjce.25304.
[25] F. Pigeonneau, D. Xu, M. Vincent, J.-F. Agassant, Heating and flow computations of an amorphous polymer in the liquefier of a material extrusion 3D printer, Additive Manufacturing 32 (2020) 101001. https://doi.org/10.1016/j.addma.2019.101001.
[26] N. Hanada, K. Higashi, Z. Zhao, K. Ueda, K. Moribe, Preparation of a ternary amorphous solid dispersion using hot-melt extrusion for obtaining a stable colloidal dispersion of amorphous probucol nanoparticles, International Journal of Pharmaceutics 640 (2023) 122959. https://doi.org/10.1016/j.ijpharm.2023.122959.
[27] P.R. Redapangu, S.P. Vanka, K.C. Sahu, Multiphase lattice Boltzmann simulations of buoyancy-induced flow of two immiscible fluids with different viscosities, European Journal of Mechanics - B/Fluids 34 (2012) 105–114. https://doi.org/10.1016/j.euromechflu.2012.01.006.